ALMA Memo 499

20 May 2004

An Approach Detecting the Event Horizon of SgrA*

Makoto Miyoshi, Seiji Kameno, José K. Ishitsuka

National Astronomical Observatory, 2-21-1 Osawa, Mitaka, Tokyo 181-8588

makoto.miyoshi@nao.ac.jp, kameno@hotaka.mtk.nao.ac.jp, pepe@hotaka.mtk.nao.ac.jp

Zhi-Qiang Shen

Shanghai Astronomical Observatory, Chinese Academy of Sciences, Shanghai 200030

zshen@shao.ac.cn

Rohta Takahashi

Yukawa Institute for Theoretical Physics, Kyoto University,

Sakyo-Ku, Kyoto 606-8502, Japan

rohta@yukawa.kyoto-u.ac.jp

and

Shinji Horiuchi

Center for Astrophysics and Supercomputing, Swinburne University of Technology,

Mail stops 31 P. O. Box 218 Hawthorn, Victoria, 3122, Australia

shoriuchi@swin.edu.au

Abstract

Imaging the vicinity of a black hole is one of the ultimate goals of VLBI astronomy. The closest massive black hole, SgrA*, located at the Galactic center is the leading candidate for such observations. Combined with recent VLBI recording technique and submillimeter radio engineering, we now have the sufficient sensitivity for the observations. Here we show performance simulations of submillimeter VLBI arrays for imaging SgrA*. Good images are obtained from submillimeter VLBI arrays in the southern hemisphere composed of more than 10 stations. We also note that even with a small array, we can estimate the shadow size and then the mass of black hole from visibility analysis. Now, all we need is to construct a submillimeter VLBI array in the southern hemisphere if we wish to unveil the black hole environment of SgrA*.

Key words: black hole, event horizon, SgrA*, submillimeter VLBI

1. Introduction

Imaging black hole system is one of the final goals in VLBI astronomy. SgrA*, the massive black hole at the Galactic center is the leading candidate for the research. This is not merely because SgrA* is the most convincing black hole candidate (Schödel et al. 2002, Ghez et al. 2000) but mainly because SgrA* shows the largest apparent angular size among black hole candidates. In table 1 we show the apparent angular sizes of Schwarzschild radii of several black hole candidates. We can recognize the SgrA* has the largest apparent angular Schwarzschild radius that is estimated to be 6μarcseconds from the mass ($2.6 \times 10^6 M_\odot$, Ghez et al. 2000) and the distance of the Galactic center (8 kpc).

As Schwarzschild radius (R_s) is proportional to the mass of the object ($R_s = 2GM_{BH}/c^2$, where G is gravitational constant, M_{BH} is the mass of black hole, and c is the light velocity), the Schwarzschild radii of what you call super massive black holes with mass more than a few $\times 10^7 M_\odot$ are really large. While the massive black holes are located at very long distance more than a few Mpc, then the resultant apparent angular sizes of theirs are not so large.

As for stellar black holes in our Galaxy located close to us, because the masses are only a few $M_\odot$, the apparent angular Schwarzschild radii tend to be quite small than those of massive black holes. For instance, a stellar black hole with $1M_\odot$ located at 1 pc has the apparent angular Schwarzschild radius of 0.02μarcseconds.

SgrA* is not so large as other massive black holes but has a mass with a few of $10^6 M_\odot$, and is located only at 8 kpc where is three order of magnitude closer than any other massive black holes. SgrA* has the largest apparent angular Schwarzschild radius of all black hole candidates (See table 1).

We cannot see a black hole itself alone in dark space. However we can expect to look the shadow of a black hole like a silhouette when the black hole is enveloped by luminous emission of jet or accreting hot matter.

The views of the black holes in the situations have been theoretically investigated. (Cunningham & Bardeen 1972, Bardeen & Cunningham1973, Cunningham 1975, Lumine 1979, Sikora 1979, Fukue & Yokoyama 1988, Perez & Wagoner 1991, Jaroszynski, Wambsganss, & Paczynski 1992, Chandrasekhar 1983, Kindl 1995, Hollywood & Melia 1995, Quien, Wehrse & Kindl 1996, Begelman & Rees 1996, Quien, Wehrse & Kindl 1996, Begelman & Rees 1996, Hollywood & Melia 1997, Bromley, Miller & Pariev 1998, Pariev & Bromley 1998, Usui, Nishida & Eriguchi 1998, Falcke, Melia, & Agol 2000, Bromley, Melia, & Liu 2001, Fukue 2003, Takahashi 2004)

The typical size of the black hole shadow is around 5 Schwarzschild radii in diameter. The finding of the shadow is, in other words, the observation of event horizon, and the perfect evidence of black hole simultaneously.

The apparent angular size of the black hole shadow of SgrA* is about 30μarcseconds

in diameter. Recent observations indicate the mass of SgrA* is $3.7 - 4.1 \times 10^6 M_\odot$ (Schödel et al. 2002, Ghez et al. 2003). If we accept the newly estimated values, the size of the black hole shadow is more than 45μarcseconds in diameter. SgrA* was detected 30 years ago (Balick & Brown 1974) and has long been recognized to be very quiet and stable source. In recent years however after the notice of quasi-periodic radio variation of 106 days in SgrA* (Zhao et al. 2001), several short time flaring events of SgrA* are unveiled. The detected rapid flares of SgrA* range from a few hours to 30 min at radio, infrared, and x-ray emissions (Miyazaki et al. 2003, Zhao et al. 2004, Genzel et al. 2003, Baganoff et al. 2001, Goldwurm et al. 2003, Porquet et al. 2003). These rapid changes strongly suggest the structural change of accretion disk or eruption of a jet in SgrA*. SgrA* has become very important for investigating black hole environment.

Not a few VLBI observations have been performed to unveil the feature of SgrA*. However the scattering effects by surrounding plasma have blurred the intrinsic image and then previous VLBI observations at lower frequencies could not reach the true face so far (Doeleman et al. 2001, Zensus et al. 1999, Bower et al. 1998, Yusef-Zadeh et al. 1994, Rogers et al. 1994, Alberdi et al. 1993, Krichbaum et al. 1993, Marcaide et al. 1992, Jauncey et al. 1989, Lo et al. 1985, 1998).

Because the scattering effect is proportional to the square of observing wavelength, the effects become negligible at submillimeter observations. To unveil the intrinsic image, we should accomplish submillimeter VLBI observations of SgrA* (Falcke et al. 2000)

In this paper we simulate the performance of submillimeter VLBI array configurations for SgrA* observations. We also note the capability of visibility analysis obtained from VLBI array composed of a few stations.

— Table 1 —

2. Simulations

We performed simulations testing array performance whether the black hole shadow can be recognized or not. Because SgrA* is located at $-30°$ in declination, the suitable array should be located at the southern hemisphere. We checked performance of three virtual arrays at the southern hemisphere, the VLBA configuration, a realistic network connecting submillimeter interferometers and so on. As image model of SgrA* we use two kinds, one is the shadow embedded at Gaussian brightness distribution, the other is the shadow centering an edge on view of accreting disk. As we focus on the performance of array configurations, the sensitivity of every station is unified. Namely the antenna diameter is 12 m with aperture efficiency 0.7. The system temperature at 230 GHz is 150 K that is attainable at the ALMA site. The observing bandwidth is 1000 MHz. Atmospheric condition is essentially important, but is neglected here.

Here we select the following 8 array configurations for the simulations.

- Array A: the same location as that of the VLBA (NRAO). Needless to say, the actual VLBA antennas have neither 230 GHz receivers nor sufficient antenna surface accuracy. This is only for configuration simulations.

- Array B: the VLBA configuration plus a virtual station located at Huancayo in Peru. The position of the virtual Huancayo antenna is situated 3375 m in altitude, just where latitude 12.0° S meets longitude 75.3° W.

- Array C: the VLBA configuration plus the Huancayo station and the ALMA in Chile where is at longitude 67.4° W by latitude 23.0° S, 5000-m in altitude.

- Array D: the VLBA plus the Huancayo station, the ALMA and the SEST (ESO) in Chile. The location of the SEST is at longitude 70.7° W by latitude 29.3° S, 2400-m in altitude.

- Array E: this array includes realistic submillimeter interferometers: namely the SMA at Mauna Kea in Hawaii, the CARMA in eastern California, the virtual Huancayo, the ALMA and the SEST (ESO) in Chile. The SMA and the SEST are now in operation, while the CARMA and the ALMA are under construction.

- Array F: the inversed VLBA, located at the southern hemisphere. Except the latitudes of stations, all other parameters are common as those of Array A.

- Array G: a virtual array located at the southern hemisphere. This array is composed of 9 stations in South America and one station at the SAAO in South Africa. The locations are listed in table 2. Except Itapetinga at Brazil other 8 stations in South America are situated at higher than 2400 m.

- Array H: a virtual array located mainly at the southern hemisphere. This array includes the array G denoted above, the SMA and the CARMA at northern hemisphere.

When the elevation of SgrA* is above 10°, each station performs the observations.

— Table 2 —

Figure 1 shows the uv coverage of the 8 arrays mentioned above at 230 GHz. The uv coverage of VLBA (Array A) is notoriously worse in north-south direction, deficient for imaging SgrA* (Fig1. a) (Bower et al 1999). Additions of stations in South America reinforce the north-south coverage of the VLBA alone (Fig.1. b, c, d). The uv coverage of Array E (a realistic submillimeter VLBI array) is wide range but quite sparse for SgrA* (Fig. 1 e).

The corresponding synthesized beams (or dirty beams) are shown in Figure 2. Also in Table 2 we show the each restoring beam size (Gaussian shape) obtained by fitting to the dirty beam during IMAGR in AIPS. While all of the FWHM of minor axes are comparable or smaller than the diameter of the black hole shadow of SgrA*, all the FWHM of major axes are larger.

— Table 3 —

The synthesized main beams (spatial resolutions) of the array B – H are about three times smaller in declination than that of array A as shown in Figure 2. The main beam of array E is certainly small but also exist quite high-level side lobes comparable to that of main beam. The arrays F, G, and H show high main beams and quite low side lobe levels.

2.2. Image models for SgrA*

Here we use two image models for SgrA*. One is a Gaussian shape with central black hole shadow (Fig.3, M). From the first VLBI observations at 215 GHz the outer size is estimated about 0.1 mas in diameter (Krichbaum et al. 1998). We adopted the value as outer diameter of the image model A. We use here the previous estimated mass of $2.6 \times 10^6 M_\odot$ (Ghez et al. 2000) and the corresponding shadow size of 30μarcseconds in diameter. The shape of the Gaussian brightness distribution is with major axis of 0.1 mas (FWHM) and minor axis of 0.08 mas (FWHM). The position angle (PA) of the major axis is 80°. This shape is after the previous VLBI observations at lower frequency that show east-west elongation of the apparent shape of SgrA*. Generally the elongation has not been interpreted as any kind of intrinsic structure but the effect of anisotropic scattering, and then the shape adopted here is only for performance tests of arrays. The central shadow shape is also the same elliptical shape with $30\mu \times 24\mu$ arc seconds, and PA=80°.

The other image model B is a type of accretion disk viewed at edge on plus very faint halo (Figure 4 (M)). This model is produced from numerical ray tracing by Takahashi (2004). The viewing angle to the disk plane is 89°. The outer diameter of the disk is $40R_s$, or 240 mas in apparent angular diameter. The spin of black hole is zero, namely this is a Schwarzschild black hole. The image shows a quite complex figure strongly affected by gravitational lensing and Doppler boosting with relativistic motion of the disk. At left side of the black hole shadow, the brightest area exists which is caused by Doppler boosting to our line of sight. While at right side the shadow seems to be slightly elongated because Doppler de-boosting harms the brightness of the area of the accretion disk. At the upside of the black hole shadow we can see the gravitationally lensed image of the opposite side of the disk. The brightest position caused by Doppler boosting is located about 14μ arc seconds east (left) from the center. The brightness of the point of symmetry is about 5.5% of that of the peak. The brightness of the faint halo is proportional to the inversed square of the distance from the center. In the Figure 4 (M) the halo shows with the 10^{-4} and 10^{-3} levels of the peak brightness by contours. The brightness ratio between the maximum to the dark halo is about 700 times.

The adopted flux density of the image models is 3 Jy which is the typical flux density of SgrA* at 230 GHz.

The second image model B is really fantastic and shows typical physical phenomena we expect at black hole vicinities. We however suppose the real image of the black hole shadow of SgrA* should be similar to the first image model A. We will discuss the issue later. The exact

frequency free from scattering effect is not sure. For example, Falcke et al. (2000) suggest the frequency is 500 GHz. We here assume the scattering effect is negligible at 230 GHz.

2.3. Resultant Images from Clean Deconvolutions

We used the AIPS (NRAO) for our simulations. We add the appropriate thermal noise for the system sensitivities when the faked visibilities are produced from the image models using UVCON in AIPS. Clean deconvolved images were produced with the task IMAGR. The restoring beams are unified to the circular Gaussian with the FWHM of 20μarcseconds which is smaller than those of the normal restoring beams shown in table 2.

Figure 3 shows the resultant images for the image model A. The produced images from the arrays A and E are not so good while other images have a dark area at the center. The array F (inverse VLBA), G and H show good images of black hole shadow. All of these arrays extend to more than 6 giga-wavelengths, and are composed of more than 10 stations mostly located at the southern hemisphere.

Array E, a network of realistic submillimeter array composed of 5 stations — SMA, CARMA, SEST, Huancayo, and ALMA — is insufficient for imaging the black hole shadow in the image model A.

Figure 4 shows the resultant images for the image model B (the edge on disk model). Every result shows the gravitationally lensed feature of the opposite side of the disk and the Doppler boosted side of the disk (= the left side of the disk) certainly. The right side of the disk that is Doppler de-boosted is also grasped vaguely. As the result the black hole shadow at the center is clearly recognized. However the thin disk portion near to our sight could not be reproduced in these results. The halo area is also recognized in every result. In the case of the F, G, and H, the circular profile of the halo is clearly shown. The image model B has a complex structure but is reproduced to some degree because the whole size is about two times larger than the size of the image model A.

Judging from the simulations the suitable arrays for imaging the SgrA* black hole shadow require more than 10 stations located at the southern hemisphere extending to 8000 km if the observing frequency is 230 GHz. Addition of stations at northern hemisphere improves the image.

We also simulated the image quality with changing the array sensitivity and found the effect of sensitivity does not show a larger difference than expected. Rather systemic phase errors from insufficient removal of delay offset and rapid phase change by atmosphere often damage the images, which is beyond our scope in this paper but must be seriously considered.

— Figure 1 —

— Figure 2 —

6

— Figure 3 —

— Figure 4 —

3. Visibility Analysis

When array has limited coverage in u-v plane, visibility analysis has been performed frequently in order to estimate the shape and size of the observed sources.

Fig. 5 shows visibility curves of three image models, (a) a simple Gaussian brightness without shadow, (b) a Gaussian with the shadow of $30\mu arcseconds(M_{BH} = 2.6 \times 10^6 M_\odot)$ and (c) a Gaussian with the shadow of $45\mu arcseconds(M_{BH} = 3.7 \times 10^6 M_\odot)$. For simplicity we used here point symmetric images.

While a Gaussian brightness distribution also shows a Gaussian curve in the visibility amplitudes, if the shadow exits the visibility function has null value points at some projected baseline length. The null value positions changes with the size of shadow. From visibility amplitude function, we can distinguish whether the shadow exists or not. Further, because the null value points move according as the shadow size, we can estimate the shadow size, and the mass of black hole from the null value positions. For measuring the correlated flux densities with uv distance, a small array composed of a few number of stations are sufficient. Extremely speaking only one VLBI baseline is sufficient to the purpose. The null value points are appear even when the source has other structures. The discussion above will become fruitful when the ture image of SgrA* is limited by other observational and theoretical circumscriptions.

— Figure 5 —

4. Discussions and Conclusions

We used the two types of image models for the simulations. Which image is appropriate for SgrA*? The spectra of SgrA* is well fitted to advection dominated accretion flows (ADAFs, Narayan et al. 1994) or radiatively inefficient accretion flows (e.g. Quataert et al. 1999, Yuan et al. 2003). It suggests that matter density around the black hole in SgrA* is quite low and then an optically thick disk is improbable (Takahashi 2004). This is not preferable to the image model B. In the case of image model B, correlated flux densities at long projected baselines are larger than those of the image model A. Because the image model B includes very high brightness point caused by Doppler boosting of relativistic velocity of the disk rotation. In other words the observed brightness temperature of SgrA* should be higher if the image is similar to the image model B. Krichbaum et al. (1998) shows that the 215 GHz correlated flux density of SgrA* at $700M\lambda$ is about 0.7 Jy, which is consistent to or lower than the predicted flux density from the image model A.

If the true image of SgrA* at submillimeter wavelength is like the image model A, from

7

visibility amplitude function with projected baseline length we can easily estimate the diameter of the black hole shadow. The mass of SgrA* range from $2.6 - 4.1 \times 10^6 M_\odot$, which is quite precise value so that we can safely forecast where the corresponding null points will appear. The first null point appears at the projected baseline ranging $1000 \sim 2000$ km in the case of image model A. If the scattering effect really becomes negligible at 230 GHz, we should put stations for submillimeter VLBI in the Andes at appropriate distance from the ALMA in order to detect the black hole shadow. The finding of the visibility null points is the first observational evidence of the event horizon of black hole.

— Table 4 —

We also check the sensitivity for the detection of the null points. In figure 4, the horizontal red line shows the 3σ r. m. s. noise level (30mJy) calculated from the condition in table 4. The accuracy of the null point measurement is about 100 Mλ at worst that corresponds $4 \sim 5\mu$ arc seconds in the diameter that gives us the accuracy of mass measurement about $3 \sim 4 \times 10^5 M_\odot$ It is obviously that we can distinguish the difference between the image model A and B.

The assumed parameters in table 4 are now in our hands using recent VLBI recording technique and submillimeter radio engineering. Last century the VLBI Giga Bit Recorder attended high-speed recording at 1 Gbps (eg. Nakajima et al. 1997, Sekido et al. 1999) and much higher recording system will appear. Even with the tandem use of the GBR system 1024 MHz bandwidth recording is attainable. Antenna and receiver systems for submillimeter observations are now in great progress for the ALMA use. Phase-up ALMA or ACA will afford great improvement of sensitivity in submillimeter VLBI. The outstanding issue for detecting the event horizon of SgrA* is whether we have some sites suitable for submillimeter observations in the Andes but away from the ALMA site. Good atmospheric conditions are required. Hence site survey at the Andes is the key point to the project.

Now, if only we find suitable sites and construct a submillimeter VLBI array in the southern hemisphere, we can unveil the black hole environments of SgrA*.

References

Alberdi, A., Lara, L., Marcaide, J. M., Elosegui, P., Shapiro, I. I., Cotton, W. D., Diamond, P. J., Romney, J. D., & Preston, R. A. 1993, A&A, 277, L1

Baganoff, F. K., Bautz, M. W., Brandt, W. N., Chartas, G., Feigelson, E. D., Garmire, G. P., Maeda, Y., Morris, M., Ricker, G. R., Townsley, L. K., & Walter, F. 2001, Nature, 413, 45

Balick, B. & Brown, R. L. 1974, ApJ, 194, 256

Bardeen, J. M., & Cunningham, C., T. 1973 ApJ, 183, 237

Begelman, M., & Rees, M. 1996, Scientific American Library, New York

Bower, G. C., & Backer, D. C. 1998, ApJ, 496, L97

Bower, G. C., Falcke, H., Backer, D. C., & Wright, M. C. 1999, in The Central Parsecs of the Galaxy, ASP Conference Series, 186, ed. H. Falcke, A. Cotera, W. J. Duschl, F. Melia, and M. H. Rieke, 80

Bromley, B. C., Miller, W. A., & Pariev, V. I. 1998, Nature, 391, 54

Bromley, B., Melia, F., & Liu, S. 2001, ApJL, 555, L83

Chandrasekhar, S. 1983, in The Mathematical Theory of Black Holes,(London:Oxford University Press), 663

Cunningham, C. T., & Bardeen, J. M. 1972, 173, L137

Cunningham, C. T. 1975, ApJ, 202, 788

Doeleman, S. S., Shen, Z.-Q., Rogers, A. E. E., Bower, G. C., Wright, M. C. H., Zhao, J. H., Backer, D. C., Crowley, J. W., Freund, R. W., Ho, P. T. P., Lo, K. Y., & Woody, D. P. 2001, AJ, 121, 2610

Falcke, H., Melia, F., & Agol, E. 2000, ApJ, 528, L13

Ford, H., C., Harms, R.,J., Tsvetanov, Z., I., Hartig, G., F., Dressel, L., L., Kriss, G., A., Bohlin, R., C., Davidsen, A., F., Margon, B., & Kochhar, A., K. 1994, ApJL, 435, L27

Fukue, J., & Yokoyama, T. 1988, PASJ, 40, 15

Fukue J. 2003, PASJ, 55, 155

Genzel, R., Schödel, R., Ott, T., Eckart, A., Alexander, T., Lacombe, F., Rouan, D., & Aschenbach, B. 2003, Nature, 425, 934

Ghez, A. M., Morris, M., Becklin, E. E., Tanner, A., & Kremenek, T. 2000, Nature, 407, 349

Ghez, A. M., Duchene, G., Matthews, K., Hornstein, S. D., Tanner, A., Larkin, J., Morris, M., Becklin, E. E., Salim, S., Kremenek, T., Thompson, D., Soifer, B. T., Neugebauer, G., & McLean, I. A. M. 2003, ApJ, 586, L127

Goldwurm, A., Brion, E., Goldoni, P., Ferrando, P., Daigne, F., Decourchelle, A., Warwick, R. S., & Predehl, P. 2003, ApJ, 584, 751

Herrnstein, J. R., Moran, J. M., Greenhill, L. J., Diamond, P. J., Inoue, M., Nakai, N., Miyoshi, M., Henkel, C., & Riess, A. 1999, Nature, 400, 539

Hollywood, J., M., & Melia, F. 1995, ApJ, 443, L17

Hollywood, J. M., & Melia, F. 1997, ApJS, 112, 423

Jaroszynski, M., Wambsganss, J., & Paczynski, B. 1992, ApJL, 396, L65

Jauncey, D. L., Tzioumis, A. K., Preston, R. A., Meier, D. L., Batchelor, R., Gates, J., Hamilton, P. A., Harvey, B. R., Haynes, R. F., Johnson, B., McCulloch, P., Moorey, G., Morabito, D. D., Nicolson, G. D., Niell, A. E., Robertson, J. G., Royle, G. W. R., Skjerve, L., Slade, M. A., Slee, O. B., Watkinson, A., Wehrle, A. E., & Wright, A. E. 1989, AJ, 98, 44

Kindl, C., 1995, Diploma Thesis (Radiation Fields of AGN-Accretion Disks), U. Heidelberg (IWR)

Kormendy, J., & Bender, R. 1999, ApJ, 522, 772

Krichbaum, T. P., Zensus, J. A., Witzel, A., Mezger, P. G., Standke, K. J., Schalinski, C. J., Alberdi, A., Marcaide, J. M., Zylka, R., Rogers, A. E. E., Booth, R. S., Ronnang, B. O., Colomer, F., Bartel, N., & Shapiro, I. I. 1993, A&A, 274, L37

Krichbaum, T. P., Graham, D. A., Witzel, A., Greve, A., Wink, J. E., Grewing, M. Colomer, F., de Vicente, P., Gomez-Gonzalez, J., Baudry, A., & Zensus, J. A. 1998, A&A, 335, L106.

Lo, K. Y., Backer, D. C., Ekers, R. D., Kellermann, K. I., Reid, M., & Moran, J. M. 1985, Nature, 315, 124

Lo, K. Y., Shen, Zhi-Qiang, Zhao, Jun-Hui, Ho, & Paul T. P. 1998, ApJL, 508, L61

Luminet, J.-P. 1979, A&A75, 228

Marcaide, J. M., Alberdi, A., Bartel, N., Clark, T. A., Corey, B. E., Elosegui, P., Gorenstein, M. V., Guirado, J. C., Kardashev, N., Popov, M., Preston, R., Ratner, M. I., Rioja, M. J., Rogers, A. E. E., & Shapiro, I. I. 1992, A&A, 258, 295

Matsumoto, H., & Tsuru, T.G. 1999, PASJ, 51, 321

Miyazaki, A., Tsuboi, M., & Tsutsumi, T. 2003, Astron. Nachr. 324, S1, 335

Miyoshi, M., Moran, J., Herrnstein, J., Greenhill, L., Nakai, N., Diamond, P., & Inoue, M. 1995, Nature, 373, 127

Nakajima, J., Kiuchi, H., Chikada, Y., Miyoshi, M., Kawaguchi, N., Kobayashi, H. & Murata, Y. 1997, in Proc. of Conf. for High Sensitivity Radio Astronomy, Cambridge Contemporary Astrophysics, 256.

Narayan, R. & Yi, I. 1994, ApJL, 428, L13

Pariev, V. I., & Bromley, B. C. 1998, ApJ, 508, 590

Perez, C. A.,& Wagoner, R. V. 1991, BAAS, 23, 945

Porquet, D., Rodriguez, J., Corbel, S., Goldoni, P., Warwick, R. S., Goldwurm, A., & Decourchelle, A. 2003, A&A, 407, L17

Ptak, A., & Griffiths, R. 1999, ApJL, 517, L85

Quataert, E., & Narayan, R. 1999, ApJ, 520, 298

Quien, N., Wehrse, R., & Kindl, C. 1996, Pour la Science, 223, 40

Rogers, A. E. E., Doeleman, S., Wright, M. C. H., Bower, G. C., Backer, D. C., Padin, S., Philips, J. A., Emerson, D. T., Greenhill, L., Moran, J. M., & Kellermann, K. I. 1994, ApJL, 434, L59

Schödel, R., Ott, T., Genzel, R., Hofmann, R., Lehnert, M., Eckart, A., Mouawad, N., Alexander, T., Reid, M. J., Lenzen, R., Hartung, M., Lacombe, F., Rouan, D., Gendron, E., Rousset, G., Lagrange, A. -M., Brandner, W., Ageorges, N., Lidman, C., Moorwood, A. F. M., Spyromilio, J., Hubin, N., & Menten, K. M. 2002, Nature, 419, 694

Sekido, M., Nakajima, J., Koyama, Y., Kurihara, N., Kiuchi, H., Kondo, T., & Kawaguchi, N. 1999, in Proc. of International Workshop GEMSTONE at CRL Tokyo, 245

Sikora, M. 1979, Acta Astronomica, 29, 87.

Takahashi, R. 2004 ApJ, submitted

Usui, F., Nishida, S., & Eriguchi, Y. 1998, MNRAS, 301, 721

Yuan, F., Quataert, E., & Narayan, R. 2003, ApJ, 598, 301

Yusef-Zadeh, Farhad, Cotton, William, Wardle, Mark, Melia, Fulvio, Roberts, & Douglas A. 1994, ApJL, 434, L63

Zensus, J. A., & Falcke, H. 1999, in The Central Parsecs of the Galaxy, ASP Conference Series, 186, ed. H. Falcke, A. Cotera, W. J. Duschl, F. Melia, and M. J. Rieke. 118

Zhao, J. -H., Bower, G. C. & Goss, W. M. 2001, ApJ, 547, L29

Zhao, J. -H., Herrnstein, R. M., Bower, G.C., Goss, W. M., & Liu, S. M. ApJL(accepted)

Table 1. Black hole mass, distance, Schwarzschild radius & shadow size

Object	Mass	Distance	Schwarzschild Radius			Shadow (diameter)
	[$M_\odot$]	[kpc]	[km]	[A.U.]	[μarcsec]	[μarcsec]
(1)	(2)	(3)	(4)	(5)	(6)	(7)
a stellar black hole	1	1×10^{-3}	2.95×10^3	1.97×10^{-8}	0.02	0.10
M82	$1.0 \times 10^{3(a)}$	3700	2.95×10^9	1.97×10^{-2}	0.01	0.05
SgrA*	$2.6 \times 10^{6(b)}$	8	7.67×10^9	5.11×10^{-2}	6.39	31.96
SgrA*	$4.1 \times 10^{6(c)}$	8	1.09×10^{10}	7.28×10^{-2}	9.10	45.48
M31	$3.5 \times 10^{7(d)}$	800	1.03×10^{11}	6.88×10^{-1}	0.86	4.30
NGC4258 (M106)	$3.9 \times 10^{7(e)}$	7200	1.15×10^{11}	7.67×10^{-1}	0.11	0.53
M87	$3.2 \times 10^{9(f)}$	16100	9.44×10^{12}	$6.29 \times 10^{+1}$	3.91	19.54

Notes. — Col. (1): Object name. Col. (2): Estimated mass of black hole. a) Matsumoto & Tsuru (1999), Ptak & Griffiths (1999), b) Ghez et al. (2000), c)Ghez et al. (2003), d)Kormendy & Bender (1999) e) Miyoshi et al. (1995), Herrnstein et al. (1999), f) Ford et al. (1994) Col. (3): Object distance. Cols. (4), (5) and (6): real Schwarzschild radius in km and in A.U., apparent angular size in μarcsec respectively. Col. (7): Apparent angular diameter (μarcsec) of black hole shadow ($=5 \times R_s$)

Table 2. Array G: station positions

Station	Latitude	Longitude	Altitude
Huancayo	$-12.0°$	$75.3°$	3375 m
ALMA	$-23.0°$	$67.4°$	5000 m
SEST	$-29.3°$	$70.7°$	2400 m
Itapetinga	$-23.2°$	$46.6°$	800 m
SAAO	$-32.4°$	$20.8°$	1760 m
Cerro Murallon	$-49.8°$	$73.5°$	3600 m
Cotopaxi	$-1.0°$	$77.0°$	5896 m
Pico Cristobal	$11.0°$	$74.0°$	5684 m
Maipo	$-34.0°$	$71.0°$	5290 m
Araral	$-21.5°$	$67.6°$	5680 m

Table 3. Restoring normal beam sizes calculated in AIPS

Array	FWHM of Major and Minor Axis	Position Angle of Major Axis
A	$76.833 \times 26.115 \mu asec$	$-2.1°$
B	$42.317 \times 24.207 \mu asec$	$24.9°$
C	$40.359 \times 22.234 \mu asec$	$41.4°$
D	$39.513 \times 20.905 \mu asec$	$48.2°$
E	$52.162 \times 15.582 \mu asec$	$42.6°$
F	$45.979 \times 31.480 \mu asec$	$5.7°$
G	$45.456 \times 31.430 \mu asec$	$64.2°$
H	$40.679 \times 19.425 \mu asec$	$47.7°$

Table 4. Parameters related to sensitivity attainable with recent technique

name	value
antenna diameter	15 m
aperture efficiency e_ϵ	0.7
system temperature	150 K
quatized efficiency $e_{q\epsilon}$	0.7
integration time	100 sec
bandwidth	1024 MHz
1σ noise level	10 mJy
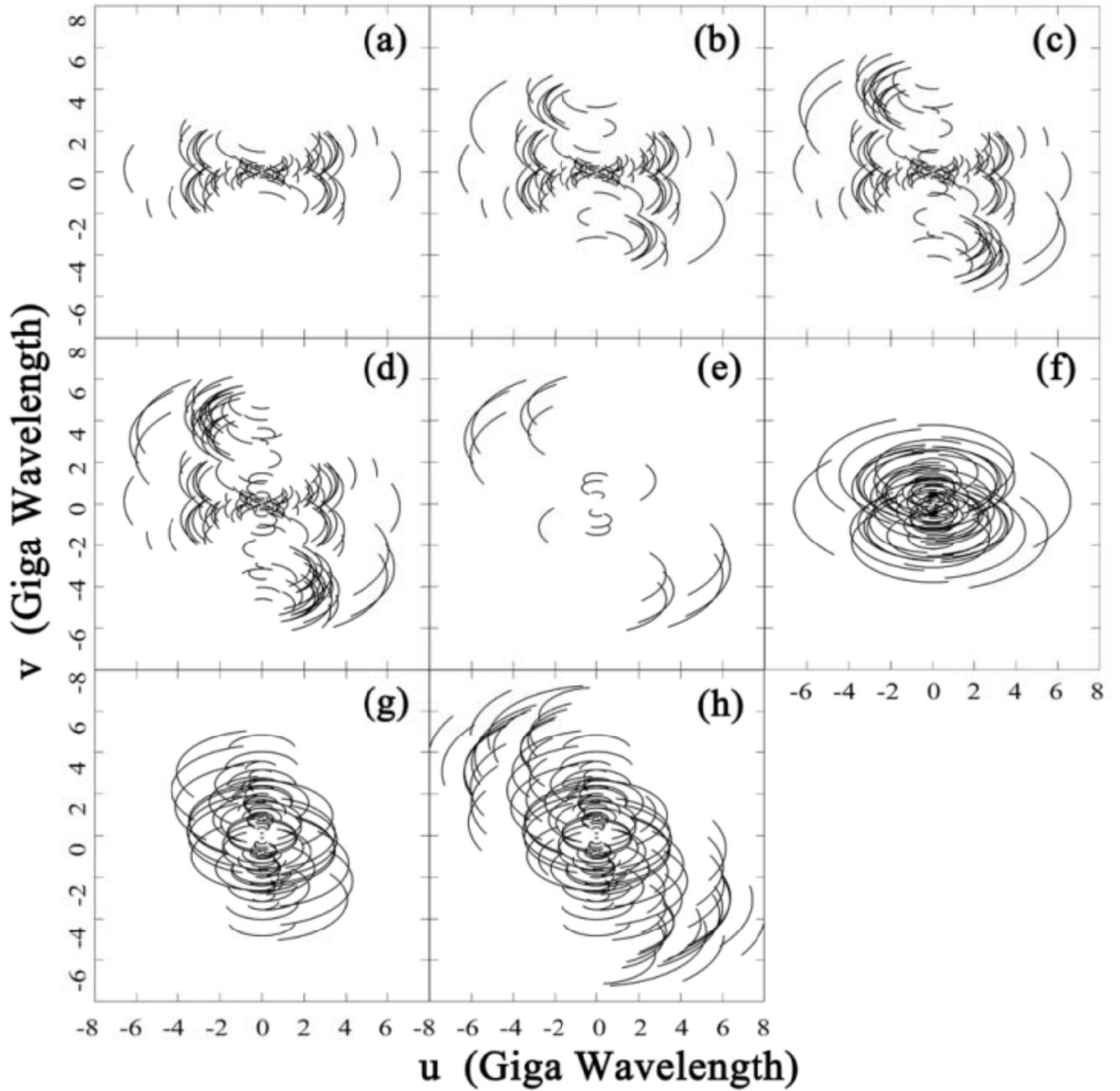
Fig. 1. The UV coverage plots of the arrays for SgrA*: (a) Array A, (b) Array B, (c) Array C, (d) Array D, (e) Array E, (f) Array F, (g) Array G and (h) Array H. The span of each side is 16 (-8 to +8) giga-wavelengths (230GHz).

14
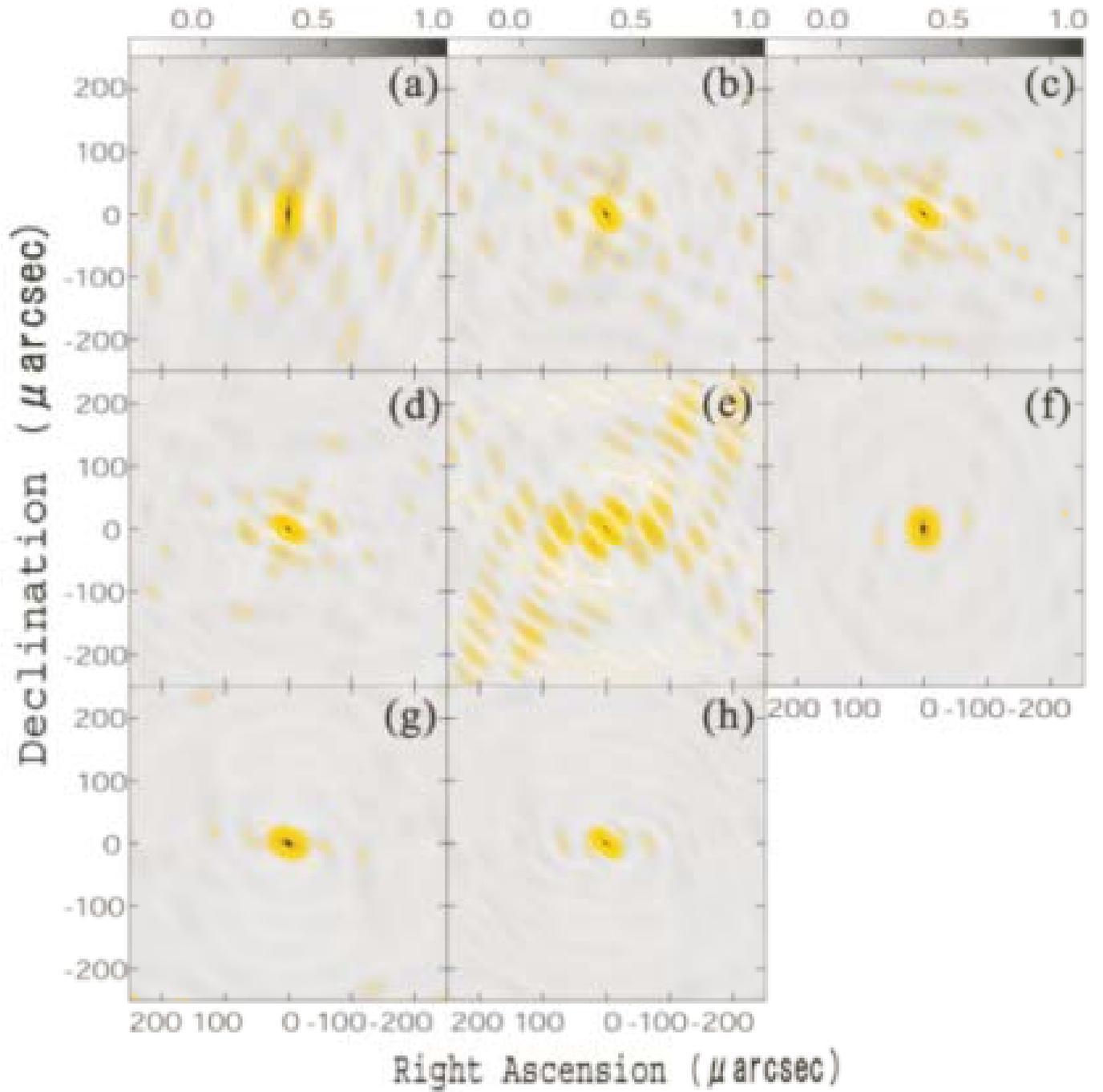
Fig. 2. The corresponding synthesized (dirty) beams: (a) Array A, (b) Array B, (c) Array C, (d) Array D, (e) Array E, (f) Array F, (g) Array G and (h) Array H. The span of each side is $500\mu asec$. The step of contours is 10% of the peak brightness.
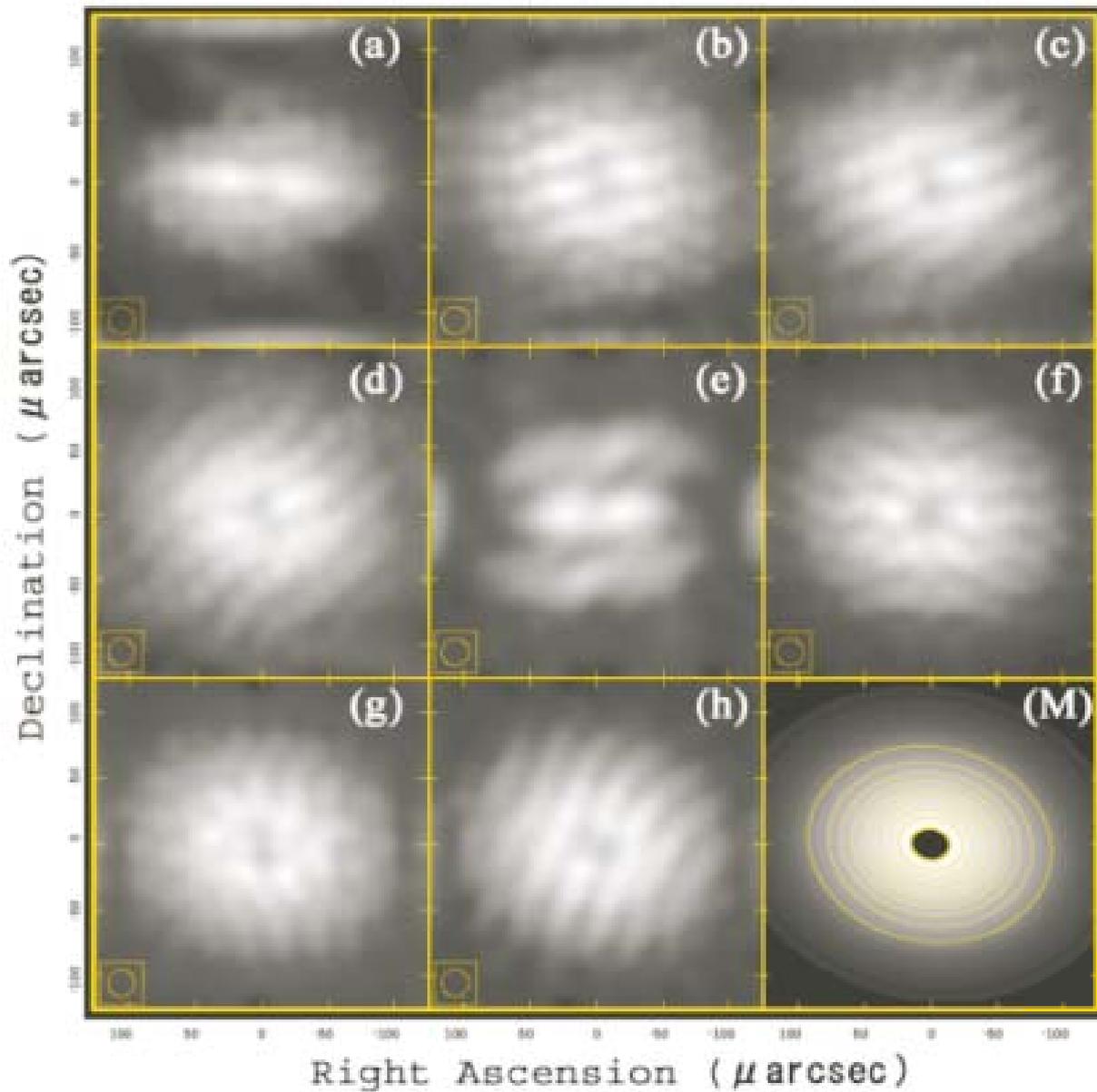
Fig. 3. Clean results from simulations for the image model A (Gaussian brightness distribution with central shadow. (a) Array A, (b) Array B, (c) Array C, (d) Array D, (e) Array E, (f) Array F, (g) Array G and (h) Array H and (M) the image model A. The span of each side is $250\mu asec$. The contour levels in the image model A (M) are 10% steps. The inset in every panel shows the used restoring beam size.

16
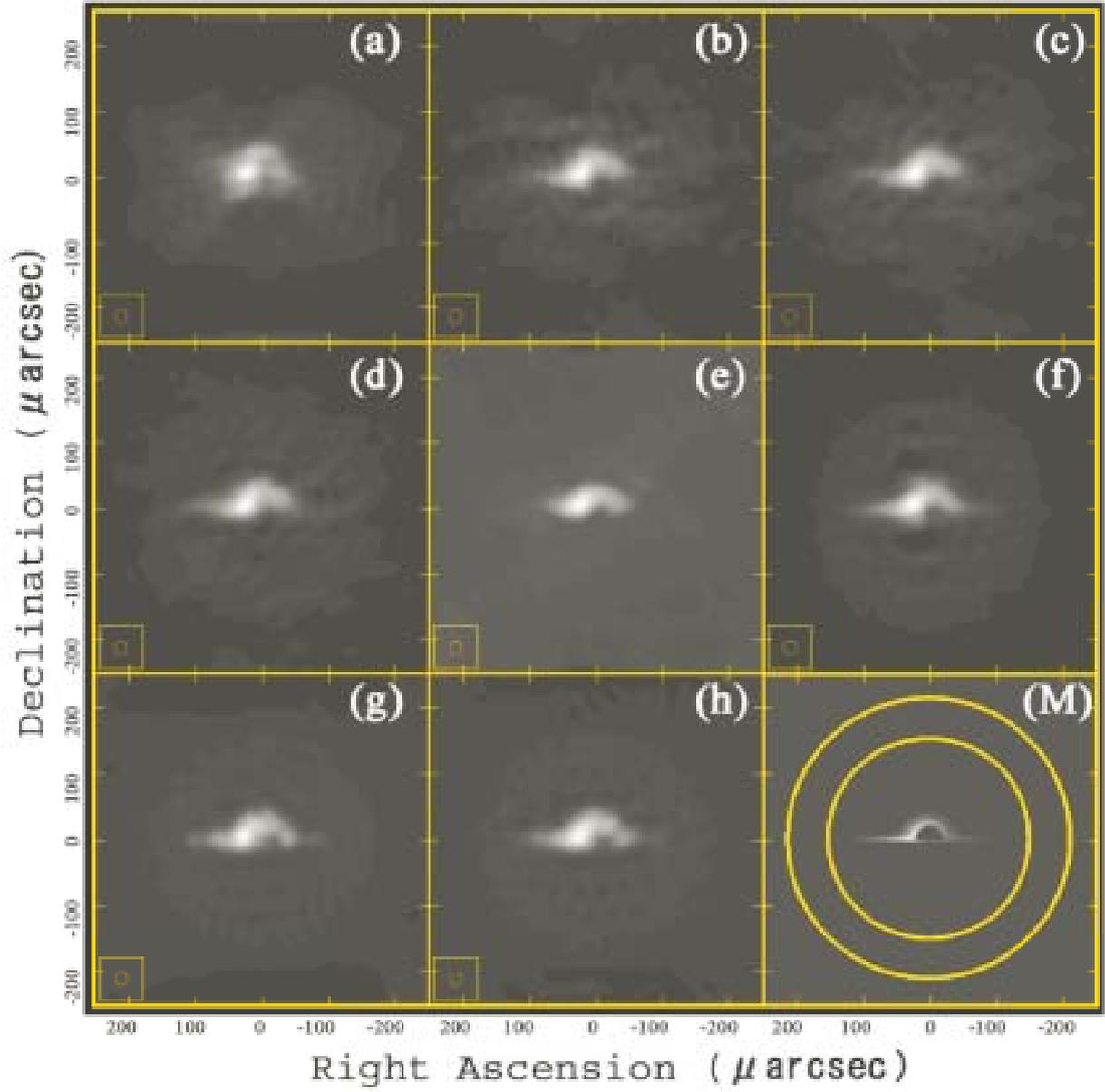
Fig. 4. Clean results from simulations for the image model B (edge on view of a standard disk plus dark halo). (a) Array A, (b) Array B, (c) Array C, (d) Array D, (e) Array E, (f) Array F, (g) Array G and (h) Array H and (M) the image model B. The two contours show 0.01% (outside) and 0.1% (inside) level of the peak brightness. The span of each side is $250\mu asec$. The inset in every panel shows the used restoring beam size.
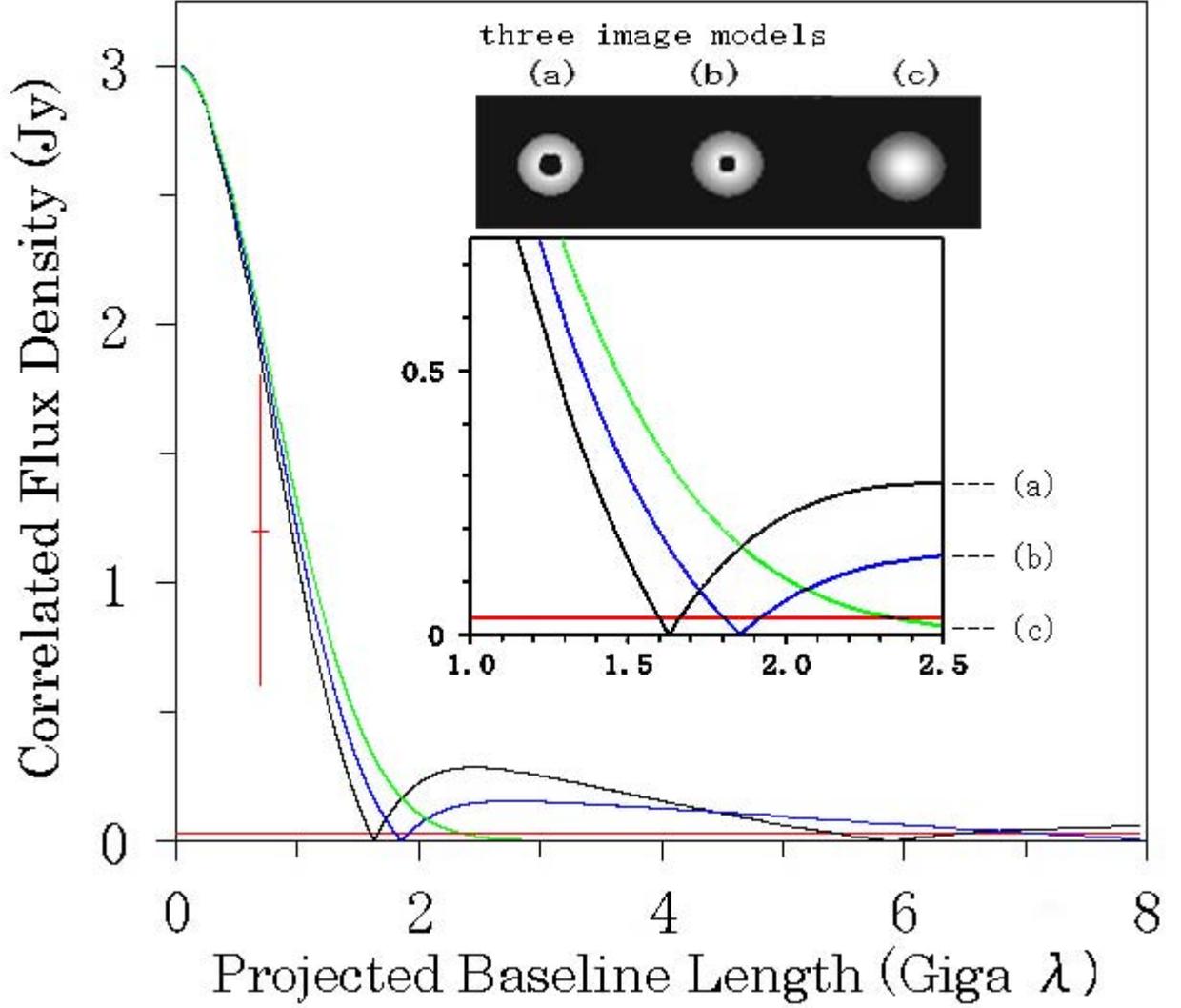
Fig. 5. The visibility amplitudes of three image models as function of projected baseline: (a) the case of $M_{BH} = 3.7 \times 10^6 M_\odot$, (b) the case of $M_{BH} = 2.6 \times 10^6 M_\odot$ and (c) the case with no black hole or the scattering effect is still dominant. The functions of (a) and (b) have null value points that indicate the existence of the central black shadow. The 3σ noise level of present engineering performance is shown by the red horizontal line. The red point with error bar is the measured visibility amplitude by Krichbaum et al. (1998)